Gene expression in the primate orbitofrontal cortex related to anxious temperament

Margaux M. Kenwood[a,b,1], Tade Souaiaia[c,1] (ID), Rothem Kovner[d], Andrew S. Fox[e] (ID), Delores A. French[b], Jonathan A. Oler[b] (ID), Patrick H. Roseboom[b] (ID), Marissa K. Riedel[b], Sascha A. L. Mueller[b] (ID), and Ned H. Kalin[a,b,f,2]

Anxiety disorders are among the most prevalent psychiatric disorders, causing significant suffering and disability. Relative to other psychiatric disorders, anxiety disorders tend to emerge early in life, supporting the importance of developmental mechanisms in their emergence and maintenance. Behavioral inhibition (BI) is a temperament that emerges early in life and, when stable and extreme, is linked to an increased risk for the later development of anxiety disorders and other stress-related psychopathology. Understanding the neural systems and molecular mechanisms underlying this dispositional risk could provide insight into treatment targets for anxiety disorders. Nonhuman primates (NHPs) have an anxiety-related temperament, called anxious temperament (AT), that is remarkably similar to BI in humans, facilitating the design of highly translational models for studying the early risk for stress-related psychopathology. Because of the recent evolutionary divergence between humans and NHPs, many of the anxiety-related brain regions that contribute to psychopathology are highly similar in terms of their structure and function, particularly with respect to the prefrontal cortex. The orbitofrontal cortex plays a critical role in the flexible encoding and regulation of threat responses, in part through connections with subcortical structures like the amygdala. Here, we explore individual differences in the transcriptional profile of cells within the region, using laser capture microdissection and single nuclear sequencing, providing insight into the molecules underlying individual differences in AT-related function of the pOFC, with a particular focus on previously implicated cellular systems, including neurotrophins and glucocorticoid signaling.

anxiety disorders | glucocorticoids | prefrontal cortex | transcriptomics | nonhuman primates

Individual differences in anxiety-related temperaments that emerge early in life can confer predisposition for either risk or resilience for the development of stress-related psychopathology. One well-established risk temperament is behavioral inhibition (BI), a temperament characterized by hyperreactivity to threat, particularly in situations involving novelty and/or uncertainty (1). Early BI is linked to a substantial increase in the risk for the later development of anxiety disorders, as well as with major depressive disorder, substance abuse, and other disorders on the internalizing spectrum (2–4). As the markers of BI emerge in childhood, this presents an opportunity for early intervention to alter the developmental trajectory that biases BI children toward developing stress-related psychiatric disorders. Effective early-life interventions are facilitated by improving the understanding of the neurobiological substrates of BI, including circuit-based and molecular alterations associated with this temperament. Additionally, given the current challenges in treating stress-related psychiatric disorders, both in children and adults, identifying novel targets for pharmacological interventions is critical.

Due to their recent evolutionary divergence from humans, rhesus monkeys share remarkable similarities in their expression of individual differences in anxiety-related temperaments (5, 6). Using a highly translationally relevant nonhuman primate (NHP) model of early BI, called anxious temperament (AT), we have characterized neural circuit alterations related to individual differences in this phenotype in young rhesus monkeys (7). AT's neural circuit encompasses subcortical regions such as the extended amygdala, anterior hippocampus, and brainstem periaqueductal gray (8). Also implicated are frontal cortical regions, including the posterior orbitofrontal cortex (pOFC), subgenual anterior cingulate cortex (sgACC), and dorsolateral prefrontal cortex (dlPFC) (9). In addition to the stability of the AT phenotype, data also support the stability of individual functional differences in components of the AT circuit, specifically amygdala metabolism (10, 11). Importantly, the AT circuit largely overlaps with the neural signatures of pathological anxiety (12) and major depression (13, 14) in clinical populations, confirming the translational relevance

Significance

Anxiety disorders, as well as other comorbid psychiatric disorders, pose a staggering burden worldwide. Currently available treatments, while effective, fail to achieve remission in a majority of patients. Novel treatments, guided by an understanding of the neurobiological substrates of anxiety disorders, would pave the way for increased efficacy in treatment and therefore improved outcomes for individuals suffering from these disorders. The studies within this paper explore the molecules associated with a highly translationally relevant nonhuman primate model for the risk for anxiety disorders, highlighting pathways that could be targeted in the treatment of anxiety.

[1]M.M.K. and T.S. contributed equally to this work.

[2]To whom correspondence may be addressed. Email: nkalin@wisc.edu.

of the NHP AT model (15). In line with current conceptualizations of anxiety, AT varies dimensionally across populations, with some individuals displaying levels of AT which are extreme relative to their peers, while others display lower levels. Therefore, this dimensional variability can be used to understand neural and molecular systems that confer either risk or protection.

Alterations in prefrontal function have been extensively associated with various psychiatric disorders (12, 16). Due to the marked similarities in cytoarchitectural, connectional, and functional properties of frontal subregions between humans and NHPs, rhesus monkeys provide an invaluable translational model with respect to understanding prefrontal contributions to stress-related psychopathology (15). Of particular interest within AT's neural circuit is the pOFC, which is posited to act as a regulator of subcortical portions of the AT circuit. Individual differences in threat-related metabolism in this portion of the PFC are associated with individual differences in AT (7). Lesions in this region alter both AT and threat-related metabolism in the neural circuitry underlying AT, particularly within the bed nucleus of the extended amygdala (BST) (17, 18), consistent with its regulatory role. Threat-related metabolism in the pOFC is coheritable with AT, suggesting that underlying genetic variability related to AT affects the threat-related function of this region (7). This region is also most densely interconnected with the amygdala, which we have posited to be at the center of the AT circuit (19, 20), with pyramidal neurons within the deep layers projecting to various subnuclei within the amygdala (21, 22) and neurons in the deep and superficial layers receiving input from the amygdala (21). Studies in rodents, focused on the analog of the primate PFC, have examined cellular and molecular mechanisms associated with responses to acute and chronic stress. These studies point to a prominent role of molecules that affect synaptic plasticity, including signaling via the glucocorticoid receptor and activation of neurotrophic receptors (23, 24), in mediating adaptive and maladaptive changes in cellular and circuit function.

Here, using transcriptomic analyses, we identify molecules in the primate pOFC that are associated with individual differences in AT. Gene expression was characterized using RNA sequencing (RNA-Seq) from RNA collected from neurons in the superficial and deep layers of the pOFC using laser capture microdissection (LCM) methods. Because of the different connectomic and functional properties of neurons within the different cortical laminae, we assessed differences in laminar transcription across neurons collected from the deep and superficial layers. Analyses focused on relating individual differences in gene expression to individual differences in AT and its components across a representative sample of preadolescent rhesus monkeys. Single nuclear RNA sequencing methods (snRNAseq) were also used to characterize transcriptionally defined cell types within the pOFC, with the goal of identifying specific subsets of neurons that might mediate the effects of AT-related molecular alterations. Together, these studies provide insights into molecular alterations within pOFC neurons that are relevant to AT and point to novel therapeutic targets related to the early-life risk for stress-related psychopathology.

Methods

AT Phenotyping. AT is assessed using a 30-min exposure to the no eye contact (NEC) condition of the human intruder paradigm (HIP) (Fig. 1*A*). Duration of freezing and reduction in the frequency of coo calls during the 30-min exposure, as well as levels of plasma cortisol following the 30-min NEC, are combined into a composite score, as described in previous publications (7, 19, 25).

Subjects. A total of 72 rhesus monkeys (*Macaca mulatta;* average age = 2.52 y, SD = 0.59, 47 males and 24 females) underwent AT phenotyping, as well as FDG-PET imaging following a 30-min exposure to the NEC, as described in

previous publications (7, 25). Animal housing and experimental procedures were conducted in accordance with institutional guidelines and were approved by the University of Wisconsin-Madison Institutional Animal Care and Use Committee. Four days after AT phenotyping, the subjects were anesthetized with ketamine, then euthanized with an overdose of pentobarbital, under the guidance of veterinary staff and in a way that was consistent with the recommendations of the Panel on Euthanasia of the American Veterinary Medical Association. Subjects were euthanized according to WNPRC guidelines that were approved by the University of Wisconsin-Madison Institutional Animal Care and Use Committee.

Laser Capture Microdissection. Following euthanasia, fresh frozen tissue was collected, flash frozen, and sectioned following previously published methods (25). Sections (14 microns thick) were taken through the extent of the pOFC, encompassing primarily posterior area 13 and the orbital pro-isocortex (OPro) and were mounted on Leica PEN (polyethylene naphthalate) LCM slides (11532918; Leica, Wetzlar, Germany). pOFC tissue was lost for one subject and, as such, LCM was performed in a total of n = 71 subjects. LCM slides were stained using a rapid stain for NeuN, which is selective for neuronal nuclei, described in more detail in ref. 25.

Dissection of deep (defined as layer V/VI) and superficial (defined as II/III) neurons was performed using a Leica LMD6500 laser capture microscope, with a targeted number of 1,000 neurons dissected from each layer per animal across 5 to 6 individual slides. Cells from the deep and superficial layers were independently pooled within each animal. For the superficial layers, staining artifact around the edges of the tissue rendered it challenging to accurately collect neurons. Thus, neurons from superficial layers were only captured for 46 animals. RNA extractions were performed using the Qiagen RNeasy Plus Micro kit (74034; Qiagen, Hilden, Germany).

RNA Sequencing of LCM-Collected Samples. RNA was sequenced at the Genome Expression Center of the University of Wisconsin-Madison. Samples were processed with Clontech SMARTer Stranded Total RNA-Seq (v2 – Pico Input) kits for library preparation. Sequencing was performed on a NovaSeq S2, with single-stranded reads targeting 100 base pairs. Reads were mapped to the RefSeq annotation (RheMac10). Alignment was performed using Sequence Alignment for Gene Expression (https://github.com/tadesouaiaia/sage) written in Python 2.7.

Model Evaluation and Differential Expression Analysis of Gene-level LCM Data. For the gene-level data, reads were aggregated across all features of the gene. Data were quantile normalized after being filtered for lowly expressed genes (genes with <1 read in 20% of the subjects). After normalization, outlier testing was performed. Three subjects in the deep layers and four subjects in the superficial layers had both low diversity and read counts, and were therefore excluded for the following analyses. The data were normalized again, following exclusion of these subjects, and a log2 transformation was applied. In genes that were expressed in at least 50% of the subjects, ordinary least squares (OLS) regressions were used to identify genes whose expression levels were associated with individual differences in AT and its components (Freezing, Cooing, Cortisol), controlling variance associated with nuisance variables related to biological and technical factors. More details about model testing can be found in *SI Appendix, Methods*.

Simulation testing was performed to determine the effects of each main predictor, controlling for the nuisance variables, on gene expression by comparing the number of predictor-associated genes with a null distribution generated from 10,000 shuffled simulations of each predictor. Empirical *P* values were calculated by determining the number of permutations that fell above the number of genes associated with each predictor, with $P < 0.05$ representing the top 5% of simulations.

Differential expression (DE) analyses were performed with the gene level data to answer several questions: 1) What genes are associated with AT and its components in gene expression data collected from the deep layers of the pOFC? 2) What genes are associated with AT and its components in gene expression data collected from the superficial layers of the pOFC? 3) What genes are differentially expressed across deep and superficial layers within the pOFC? 4) What genes are differentially expressed with respect to sex? and 5) What genes are differentially expressed within the pOFC, controlling for laminar identity? Analyses were performed in a custom pipeline written in python 2.7, as well as in limma (26).

GO Ontology analyses were performed using the Functional Mapping and Annotation tool (https://fuma.ctglab.nl/) and using the statistical enrichment tool in the Pather Database (https://www.pantherdb.org/panther/ontologies.jsp).
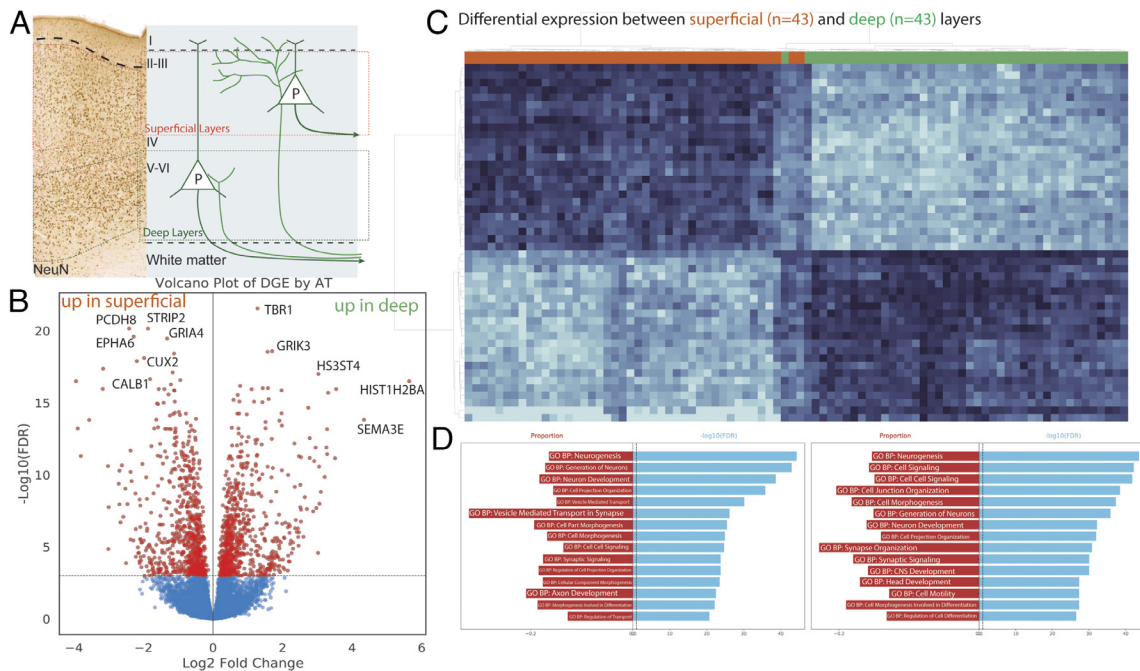
Fig. 1. Differences in transcription between the deep and superficial layers of the pOFC. (*A*, *Left*) Immunolabeling of the distribution of NeuN+ neurons within the pOFC, with the cortical surface at the top and white matter (WM) at the bottom of the image. Deep and superficial layers are demarcated with green and orange dotted lines, respectively. (*Right*) Schematic showing the primary projection patterns of deep and superficial pyramidal neurons, with deep-layer neurons primarily targeting subcortical structures and superficial neurons primarily targeting intracortical targets. (*B*) A volcano plot showing differential expression between deep and superficial layers, with the log2 fold change score on the *x* axis and −log$_{10}$(FDR-corrected *P*) on the *y* axis. Genes of interest are labelled. The dotted line shows a cutoff of −log$_{10}$(FDR-corrected *P*) < 0.001, with all genes passing that threshold shown in red dots. (*C*) A heatmap showing expression of the top 200 differentially expressed transcripts between deep and superficial layers, all of which survive FDR correction at *P* < 0.05. Genes are hierarchically clustered along the *y* axis, parsing into genes either up-regulated in the deep or superficial layers. Samples are also hierarchically clustered along the *x* axis, with all samples taken from the deep and superficial layers clustering together, respectively. (*D*) Ontology analyses performed on all transcripts that survive FDR correction show that several pathways are enriched in genes up-regulated in either superficial or deep layers. The blue bar shows the −log$_{10}$(FDR-corrected *P*) for the ontology enrichment, with the dotted line showing a cutoff of FDR-corrected 0.05, while the red bar shows the proportion of the genes in the category that are represented in the DGEs.

Enrichment was assessed by inputting a list of genes that were associated with the predictor of interest at *P* < 0.05 corrected values. Statistical overrepresentation tests were performed with respect to a background set that contained all genes within the *Macaca mulatta* transcriptome. Fold enrichment statistics and their corresponding p value were reported for all enriched pathways in *SI Appendix*, Table S2.

Single Nuclear Dissociation and Sequencing. Using the subjects with the four highest and four lowest AT scores from the n = 71, we performed single nuclear sequencing. Tissue was dissected from the pOFC, using the same slab from which neurons were collected by LCM. Prior to nuclear extraction, RNA integrity was tested on tissue collected from the slab, to verify that the LCM procedure had not substantially degraded the RNA. A cutoff RIN of 6.0 was applied. In a cryostat at −8C, 20-micron sections were collected and stained for NeuN and AchE, using previously described protocols (25) to confirm the correct anatomical location. Furthermore, several 14-micron sections were collected and mounted on SuperFrost+ for in situ validation of transcripts of interest.

Once the anatomical location was verified, the pOFC was dissected using a chilled scalpel at −20C. The dissected tissue was placed in a 1.5-mL tube chilled on methanol and dry ice and then processed following protocols adapted from ref. 27 (more details in *SI Appendix*). Dissociated samples were processed using a 10× 3′ Single Cell v3.1 RNAseq kit, per the instructions of the manufacturer at the University of Wisconsin–Madison Gene Expression Center. Sequencing was performed using a NovaSeq S2, with each sample divided across two flowcells, in two rounds. Reads were converted from .bcl2 files to .fastq files using the cellranger mkfastq command.

Alignment, Quality Control, and Analysis of Single Nuclear Data. Reads were aligned to the RheMac10 genome using cellranger, with the recommended modifications for compatibility of the genome. Demultiplexing on reads was performed, collapsing reads with the same unique molecular identifier (UMI) into a single count, to account for the amplification bias inherent to single-cell

sequencing protocols due to the low input RNA (28). Cells were excluded based on two criteria: 1) >5% of expression from mitochondrial RNA and 2) expression of less than 200 genes. Data were filtered for doublets using Scrublet (29), which resulted in the exclusion of 9,687 cells. The counts were normalized and log2 transformed by subject, then integrated using scanorama (30). The final counts file was analyzed using Scanpy (31) with methods detailed in *SI Appendix*, *Materials*.

RNAscope. Fresh frozen hemisected brain tissue was sectioned at 20 mm and mounted on Superfrost plus slides and stored at −80C. In situ hybridization was performed as instructed by the manufacturer of RNAscope® Multiplex Fluorescent Reagent Kit v2 catalog 323110 (Advanced Cell Diagnostics). Upon removal from the −80C, the sections were dried at −20C for 60′ before postfixing in prechilled 4% PFA in 1× PBS for 15 min at 4 °C. The sections were washed, dehydrated, and dried before being treated with H$_2$O$_2$. Sections were treated with protease prior to incubation with custom RNAscope probes designed to detect CALD1 or NR3C1. Following several amplification steps, the probes were detected using either Opal 570 or Opal 650 reagents (Akoya Biosciences).

Stack images were acquired using a Nikon A1R+ Confocal (Biochemistry Optical Core, University of Wisconsin, Madison). Images were preprocessed using ImageJ version 1.53s and CellProfiler version 4.2.1. Cell numbers and probe detections were collected using QuPath software v0.4.3.

Results

Sample Characterization and Phenotyping. The sample of n = 72 was drawn from a larger subset of subjects that underwent phenotyping in the NEC condition of the HIP. As one subject was missing the brain slab containing the pOFC, neurons were collected from a total of n = 71 subjects. The sample of n = 71 included in this study comprises both male (n = 47) and female

(n = 24) subjects in the periadolescent age range (Age = 2.56 ± 0.71 y). Several of the subjects included in this study underwent repeated phenotyping in the NEC condition either two (n = 48) or three (n = 24) times. AT scores were stable (r's ranging from 0.76 to 0.96) across the repeated testing (*SI Appendix*, Fig. S2*A*) which is comparable to r values from previous studies in our lab assessing AT's stability across time (32, 33) and consistent with the interpretation of AT as trait. For each subject, we selected the AT score that was closest to the time point at which the brains were collected as our primary outcome of interest.

To verify that this LCM sample was representative, we compared AT scores calculated across a larger population (n = 721) in which we performed AT phenotyping to the AT scores calculated within the current sample (n = 71). The n = 71 subjects that formed part of the LCM study did not differ in terms of their distribution as compared to the sample of n = 721 (Mann–Whitney U = 24,062, P =0.4), demonstrating that this sample was representative of the larger population with respect to AT (*SI Appendix*, Fig. S2*B*).

Differential Expression between Deep and Superficial Layers. Within the pOFC cortical laminae (Fig. 1*A*), pyramidal neurons residing in the superficial layers (Layers II/III) primarily send feedforward projections to other cortical regions, while pyramidal neurons in the deep layers (Layers IV/V) primarily send feedback projections to cortical and subcortical regions (34–37). Prior work using both bulk and single-cell transcriptional characterization has shown that in addition to differing in terms of their connectivity, deep and superficial neurons differ in their transcriptional properties (38–40). After quality control, where n=3 subjects were excluded due to low library complexity, n = 68 subjects remained for analysis. Due to staining artifacts that primarily affected the outer edge of the tissue, neurons from the superficial layers were only collected from a subset of the subjects. The following analyses were performed on the subset of subjects (n = 43; n = 30 males, n = 13 females) from which both deep and superficial neurons were collected.

To characterize the transcriptional variation within the dataset, a principal components analysis was performed on the combined quantile normalized data (*SI Appendix*, Fig. S1*C*). The top principal components were correlated with predictors and nuisance variables of interest. As anticipated, the first principal component (PC1) was strongly correlated with layer identity (Region, r = 0.93, see *SI Appendix*, Fig. S1*D*), as well as with the number of cells collected (r = 0.64), which differed across layers (F(1,82) = 88.66, P <0.0001, partial eta squared = 0.52), with more cells collected in deep than superficial layers. Because of the significant difference between the number of cells collected across layers, we statistically controlled for this variable in all models. Together, these analyses suggest that there is substantial variability in gene expression associated with layer identity.

To determine the transcripts that were driving this variation across the neurons collected from deep and superficial layers, we performed DE analyses between deep and superficial layers, the results of which are visualized in a heat map in Fig. 2*B*. Hierarchical clustering demonstrated that in general, samples clustered together with other samples from the same layer (superficial in green, deep in orange). There were 5,173 transcripts that were significantly associated with layer identity at P < 0.05 uncorrected, 3,543 of which survived FDR correction at q < 0.05. Of these genes, 1,714 genes (48.37%) were up-regulated in superficial layers, while 1,829 genes (51.62%) were up-regulated in deep layers (Fig. 1*B*).

Pathway analyses of DE genes surviving FDR correction for genes up-regulated in deep layers demonstrated these genes were enriched in several Gene Ontology (GO) categories, including the opioid prodynorphin pathway (P05916, fold enrichment = 3.35, FDR-corrected P = 0.045), beta 1 adrenergic receptor signaling (P04377, fold enrichment = 2.91, FDR-corrected P = 0.04) and beta 2 adrenergic receptor signaling pathway (P04378, fold enrichment = 2.98, FDR-corrected P = 0.04), metabotropic glutamate receptor group II pathway (P00040, fold enrichment = 3.04, FDR-corrected P = 0.036), dopamine receptor-mediated signaling pathway (P05912, fold enrichment = 2.59, FDR-corrected P = 0.05), and others shown in *SI Appendix*, Table S2. GO terms that were overrepresented in genes up-regulated in the superficial layers included metabotropic glutamate receptor group I pathway (P00041, fold enrichment = 4.81, FDR-corrected P = 0.003), insulin/IGF pathway-protein kinase B signaling cascade (P00034, fold enrichment = 3.64, P = 0.002), and others described in *SI Appendix*, Table S2.

There are several potential contributions to the marked differences in transcriptional profile across the lamina. First, pyramidal neurons within the deep and superficial layers have been shown to differ in terms of their functional properties, particularly with respect to apical dendrite function (41–43). Many of the ontology categories that were enriched in differentially expressed genes were receptors, which could help to explain the different physiological properties of these cells. A second contributor is differences in the admixture of cell types collected across the deep and superficial layers. The rapid NeuN staining protocol that was used to identify cells for laser capture microdissection stained for both excitatory and inhibitory neurons and, as such, both were collected. Thus, some of the differences across layers could result from the differing proportions of cell types constituting the layers.

To determine the extent to which these findings are consistent with prior work assessing differential expression between cortical laminae, this list of differentially expressed genes was compared that from the NIH Blueprint NHP Atlas Microarray Data (https://www.blueprintnhpatlas.org/). These data were used to calculate differential expression between superficial layers (layers 2 and 3) and deep layers (layers 5 and 6) in the medial OFC of adult rhesus monkeys, the area most comparable to the pOFC region used in our current study. Of the 863 probes that were up-regulated in superficial layers in the NHP Atlas microarray data, 239 transcripts (27.7%) were also up-regulated in our data. Of the 579 probes that were up-regulated in deep layers in the NHP Atlas microarray data, 418 transcripts (72.19%) were also up-regulated in our data. Because microarray data is limited to a set of preselected probes, our data not only extends the microarray data to a larger sample (n = 43 in the current study, n = 3 in the NHP Atlas), but by using RNAseq, provides a more comprehensive characterization of transcriptomic differences between deep and superficial layers of the primate OFC.

Together, these results confirm the well-established molecular differences between deep and superficial layers and demonstrate the importance of exploring AT-related variation in these regions separately.

The Relationship between AT, Its Components, and Gene Expression in the Deep and Superficial Layers.
Molecular substrates of AT and its components in the deep and superficial layers. To test the main effect of AT and its components on transcriptome-wide expression, we used permutation testing to generate a null distribution (n = 10,000 permutations) and independently compared the number of genes associated with AT and its components (freezing, cooing, and cortisol) to the median of the null distribution for the corresponding layer. This analysis allowed us to determine whether the predictor performed better than would be expected by chance (Fig. 2), providing an omnibus statistic to justify further exploration of the genes driving the transcriptome-wide effect. Within the deep layers, AT had a significant effect on
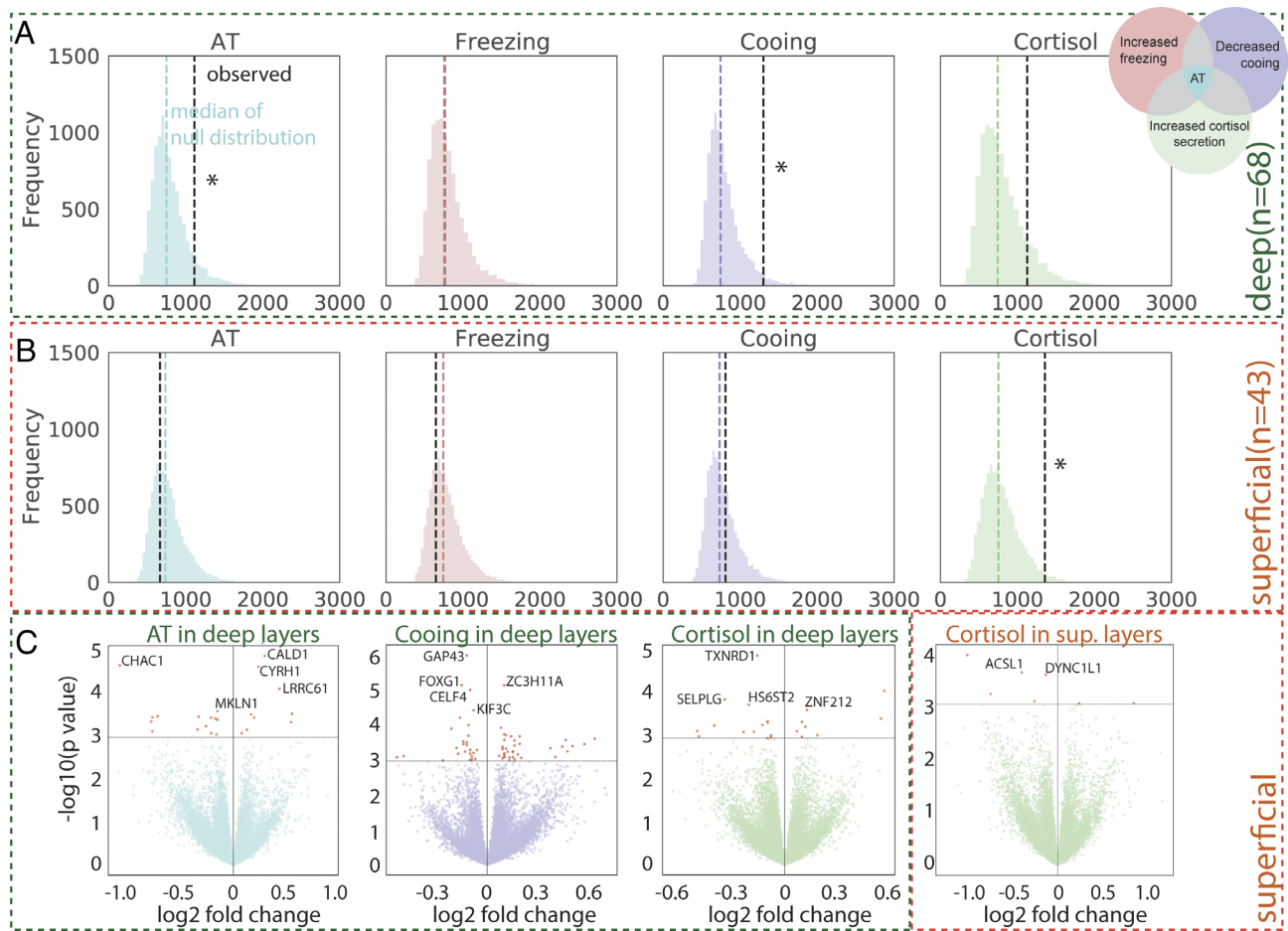
Fig. 2. AT, cortisol, and cooing are associated with transcriptome-wide expression in either the deep or superficial layers of the pOFC. (*A* and *B*) Permutation testing (n = 10,000 permutations) was performed to determine the performance of each main predictor relative to a simulated null distribution, which is shown for each predictor as a histogram (AT in blue, freezing in pink, cooing in purple, and cortisol in green) for the deep (*A*) and superficial (*B*) layers. The median of the distribution is shown with a colored dotted line, while the actual number of genes associated with each predictor is shown by a black line. Empirical *P* values were calculated for AT and each of its components (shown in the *Inset*): AT: *P* = 0.048, freezing: *P* = 0.24, cooing: *P* = 0.019, cortisol: *P* = 0.07 in deep layers (green); AT: *P* = 0.32, freezing: *P* = 0.35, cooing: *P* = 0.17, cortisol: *P* = 0.015 in deep layers (orange). * indicates a significant empirical *P* value. (*C*) For all predictors that with empirical *P* values < 0.1 in the permutation testing, a volcano plot showing differential expression with respect to that predictor is shown. Outlined in green, volcano plots for AT (green), cooing (purple), and cortisol (green) are shown, with the log2 fold change score on the *x* axis and −log$_{10}$(uncorrected *P* value) on the *y* axis. Genes of interest labelled. The dotted line shows a cutoff of −log$_{10}$(uncorrected *P* value) < 0.001, with all genes passing that threshold shown in red dots.

transcriptome-wide expression (empirical *P* = 0.0483). Of AT's components, cooing (empirical *P* = 0.0196) performed better than would be expected at chance, with cortisol nearing significance (empirical *P* = 0.07). Within the superficial layers, AT did not perform better than chance (empirical *P* = 0.32). Of AT's components, only cortisol performed better than chance (empirical *P* = 0.0147) in the superficial layers. For predictors with evidence for a transcriptome-wide effect on gene expression (see *SI Appendix*, Fig. S1 for a schematic of the analysis pipeline), DE was assessed using an ordinary least squares regression on the log normalized gene expression values. Ontology analyses were performed on transcripts associated with each predictor at *P* < 0.05 uncorrected.

Transcripts and ontology categories associated with AT and its components.

i. AT. Within the deep layer set, AT was associated with the expression of 995 transcripts (*P* < 0.05 uncorrected). Among the top 50 transcripts associated with AT were several interesting genes, including Cysteine and histidine rich 1 (CYHR1: t value = 54.59, *P* < 0.0001 uncorrected), a protein that binds zinc and galectin-3, whose cellular function has not been well characterized. Expression of *CYHR1* in corticolimbic regions has previously been implicated in differences in defensive responses across rodent strains (44). Muskelin 1 (*MKLN1*) was inversely associated with

individual differences in AT. Deletion of this gene in rodents has been shown to decrease dendritic spine stability and branching (45) and was also linked to early-onset bipolar disorder in a recent GWAS (46). Neural cell adhesion molecule 1 (NCAM1) was positively associated with individual differences in AT. *NCAM1* has been implicated in synaptic stability and plasticity (47), as well as being linked to various neuropsychiatric disorders (48, 49). A complete list of AT-associated genes, and their associated statistics, can be found in *SI Appendix*, Table S1.

Several ontology pathways were enriched in the differentially expressed genes at FDR-corrected levels, including cellular response to stress (GO:0080135, *P* < 0.0001), methylation (GO:0032259, *P* < 0.0001), and other terms found in *SI Appendix*, Table S2. Interestingly, one of the enriched terms for AT-associated transcripts was the steroid hormone–mediated signaling pathways (GO: 0043401, *P* = 0.045), a category which includes the transcript for the glucocorticoid receptor (*NR3C1*), a receptor with well-established links to corticosteroid-mediated alterations in cellular function and transcription (50). The transcript for the glucocorticoid receptor (*NR3C1*) was inversely associated with AT (R^2 = 0.224, *P* = 0.03, Fig. 3*C*), such that animals with high AT displayed lower levels of the transcript for this receptor. In addition to steroid hormone–mediated signaling, AT-related genes were also enriched other ontology

categories related to glucocorticoid signaling, including transcripts identified in a prior study that performed sequencing in lymphoblasts after extended glucocorticoid exposure (FDR-corrected $P = 0.047$, ref. 51), as well as for genes containing GRE binding elements within their upstream promoter region (M12784, FDR-corrected $P = 0.023$). The glucocorticoid receptor (GR), which is activated by cortisol that is released from the adrenal cortex as part of stress-related HPA axis activation (52–54), has been extensively implicated in mediating cellular responses to stress. GR signaling leads to both long- and short-term changes in cellular signaling, through intracellular cascades and through nuclear translocation, where the activated GR can bind to and directly affect changes in gene expression (55, 56).

While there is a well-established link between the GR and stress, our study identified a GR-related transcript of interest: The expression of *CALD1*, which encodes caldesmon, an actin-binding protein which is named for its ability to bind calmodulin (57), was the transcript with the strongest association with AT ($R^2 = 0.313$, $P < 0.001$, Fig. 3D). Although not extensively studied in the brain, caldesmon has been studied in the context of muscle cells, where it acts as a dynamic cross-linker of myosin and tropomyosin fibers, promoting cell motility and other critical functions (58). Interestingly, *CALD1* expression is regulated by GR signaling in the presence of glucocorticoids (59, 60), affecting the stability of the actin cytoskeleton (61), mobility of cells (62), and dendritic spine development (60). *CALD1* was only associated with AT in the deep layers, suggesting that its plasticity-promoting effects may be targetable to deep-layer neurons. The transcript for Phosphatidylinositol-4,5-bisphosphate 3-kinase catalytic subunit alpha (*PIK3A*), which activates protein kinase B (*AKT*) via phosphorylation, was inversely associated with AT.

PIK3CA has been shown to interact with the GR, mediating intracellular cascades following inflammation (63).

ii. *Threat-related cortisol.* Individual differences in threat-related cortisol were associated with 1,061 transcripts ($P < 0.05$ uncorrected) in the deep layer dataset. Within the superficial layers, 1,283 transcripts ($P < 0.05$ uncorrected) were associated with individual differences in threat-related cortisol. Cortisol was the only component of AT that was significantly related to gene expression in both the deep and superficial layers. Of the top 50 transcripts associated with threat-related cortisol at uncorrected levels in deep layers, several interesting transcripts were represented. Levels of the transcript for thioredoxin reductase 1 (TXNRD1, t = –4.79, uncorrected $P < 0.0001$), a key enzyme that protects against oxidative stress and has previously been linked to PTSD in humans (64, 65), were inversely associated with threat-related cortisol levels. Heparan sulfate 6-O-sulfotransferase 2 (HS6ST2, t = –4.02, uncorrected $P = 0.0002$), a gene on the X chromosome which has previously been linked to trait neuroticism in the UK Biobank (Luciano et al.), was also inversely associated with threat-related cortisol levels. In the superficial layers, threat-related cortisol was inversely associated with acyl-CoA synthetase long chain family member 1 (ASCL1, t = –4.05, uncorrected $P = 0.0002$) and Cytoplasmic dynein 1 intermediate chain 1 (DYNC1I1, t = –4.01, uncorrected $P = 0.002$). A complete list of cortisol-associated genes, and their associated statistics, can be found in *SI Appendix*, Table S1.

Pathways enriched (at $P < 0.05$ uncorrected) within the differentially expressed genes related to cortisol in the deep layers included regulation of catabolic processes (GO:0009894, $P < 0.0001$), diseases of signal transduction by growth factor receptors
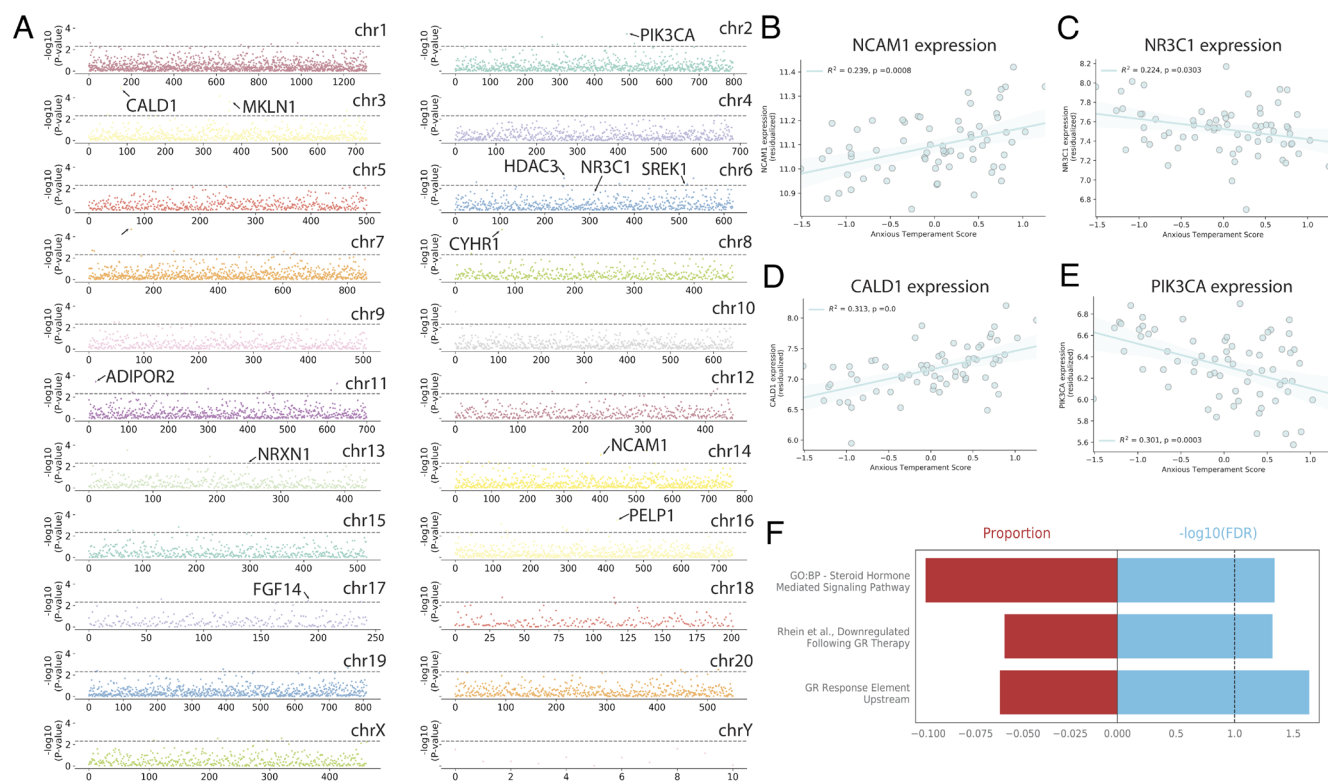

Fig. 3. RNA sequencing of deep-layer neurons in the pOFC reveals transcriptome-wide associations with AT. (*A*) A Manhattan plot displaying the −log10 *P* value, corrected using gene-level permutation testing. As can be seen, transcriptome-wide alterations are associated with individual differences in AT. Genes of interest are highlighted in the plot. The dotted line shows a threshold of $P < 0.001$ uncorrected. NR3C1 is also highlighted, as it is discussed in the text. (*B–E*) Correlations between (*B*) NCAM1, (*C*) NR3C1, (*D*) CALD1, and (*E*) PIK3CA mRNA expression levels and AT. mRNA expression levels are presented as quantile normalized log2 transformed values residualized for age at necropsy, sex, and RIN. (*F*) AT-associated genes are enriched for several GR-related ontology categories, shown in the bar plot. The blue bar shows the −log$_{10}$(FDR-corrected *P*) for the ontology enrichment, with the dotted line showing a cutoff of FDR-corrected 0.05, while the red bar shows the proportion of the genes in the category that are represented in the DGEs.

and second messengers signaling pathway (M27547, $P < 0.0001$) and Alzheimer's Disease (WP5124, $P < 0.0001$). Interestingly, and consistent with prior literature, the genes that were associated with threat-related cortisol in the deep layers were enriched in the brain-derived neurotrophic factor (BDNF) signaling pathway (WP2380, fold enrichment = 3.96, $P < 0.0001$), a finding discussed in more depth in the following paragraph. In the superficial layers, genes associated with cortisol were enriched in the interleukin 6 (IL6) signaling pathway (WP364, $P = 0.0019$), an interleukin that has been linked to immune responses in the brain (66) and transforming growth factor (TGF) beta signaling pathway (WP366, $P = 0.021$). TGFbeta is a neurotrophic factor with a demonstrated role in synaptic plasticity (67).

The enrichment of the BDNF signaling pathway in the deep layers for the cortisol-associated transcripts is of particular interest. BDNF is a member of the neurotrophin family, which comprises several tyrosine kinase receptors that dimerize in the presence of their ligands and promote plasticity processes via intracellular signaling and transcriptional mechanisms. BDNF primarily binds to neurotrophin receptor kinase 2 (NTRK2) signaling via this pathway has been extensively linked to cellular plasticity in medial frontal neurons in rodent models of chronic stress (24, 68). This finding is consistent with our previous work, which has implicated the neurotrophin tyrosine kinase receptor 3 (NTRK3) within the dorsal amygdala as a mediator of individual differences in AT (69). Importantly, manipulations in the dorsal amygdala of NHPs involving viral vector-mediated overexpression of the ligand for NRTK3, neurotrophin 3 (NT3), support a mechanistic role for this neurotrophin system in AT and its neural circuit.

iii. *Threat-related inhibition of vocalizations.* Threat-related inhibitions in vocalizations were associated with transcriptome-wide expression in the deep but not superficial layers (Fig. 2 *A* and *B*). In the deep layers, individual differences in the tendency to inhibit affiliative vocalizations during NEC were associated with 1,425 transcripts ($P < 0.05$ uncorrected), four of which survived FDR correction (Fig. 2C). The transcript for growth-associated protein 43 (GAP43) was positively associated with inhibition of vocalizations (t = −5.47, FDR-corrected $P = 0.014$), suggesting increased expression of this transcript with respect to higher levels of temperamental anxiety. GAP43 encodes for a protein involved in synaptic plasticity, which when knocked out in mice, decreases social behavior (70). Threat-related inhibition of vocalization was also inversely associated with forkhead box P1(FOXP1) (t = −4.94, FDR-corrected $P = 0.034$) and CUGBP Elav-Like Family Member

4 (CELF4) (t = −4.85, FDR-corrected $P = 0.035$) and positive associated with FOXG1 (t = 4.93, FDR-corrected $P = 0.034$). A complete list of cooing-associated genes, and their associated statistics, can be found in *SI Appendix,* Table S1. With respect to ontology, the genes associated with inhibited vocalizations included neurogenesis (GO:0022008, stats), positive regulation of transcription via RNA polymerase II (GO:0045944, stats), and BDNF signaling pathway (WP2380, stats).

Associations between Gene Expression and Sex. AT is typically assessed between 2 and 3 y of age, a developmental time point that precedes the onset of puberty. In our large sample (n = 592), we do not observe differences in AT across sex (7). However, this does not preclude the possibility that differences in gene expression at this time point can confer vulnerability to or protection from the effects of pubertal hormones. Because of the size of the sample and mixed-sex composition (n = 48 males and n = 23 females), we explored the main effect of sex on prefrontal gene expression within these data. As in our large sample, there was not a statistically significant difference in AT between males and females (t = −0.07, $P = 0.94$) in the sample of n = 72.

Permutation testing revealed that there was an effect of sex on gene expression in the deep but not superficial layers of the pOFC (Fig. 4A). DE analyses revealed that 1,358 transcripts were differentially expressed at $P < 0.05$ uncorrected, 27 of which survived FDR correction (Fig. 4B). Among these, several transcripts that are encoded on sex chromosomes and have a well-established link to sex differences (ZFY, KDM5D, UTY, TBL1Y, and USP9Y) were up-regulated in males, while others were up-regulated in females (DDX3X, KDM5C), shown in the volcano plot in Fig. 4B. Many of the sex-linked transcripts identified in this analysis act as regulators of transcription, particularly in the context of early developmental patterning (71). For example, the top differentially expressed gene, KDM5D, which was up-regulated in males encodes a histone demethylase which has been shown to regulate development and synapse formation in the neuromuscular junction of *Drosophila* (72). Many of the differentially expressed genes that were up-regulated in males were from the male-specific portion of the Y chromosome, which included mostly genes with known homologues on the X chromosome (e.g., KDM5C/KDM5D, DDX3X/DDX3Y, and others in Fig. 4B).

Finally, a linear model testing the interaction between sex and AT was used to identify transcripts with different relationships between AT in males and females (Fig. 4C). The transcript for
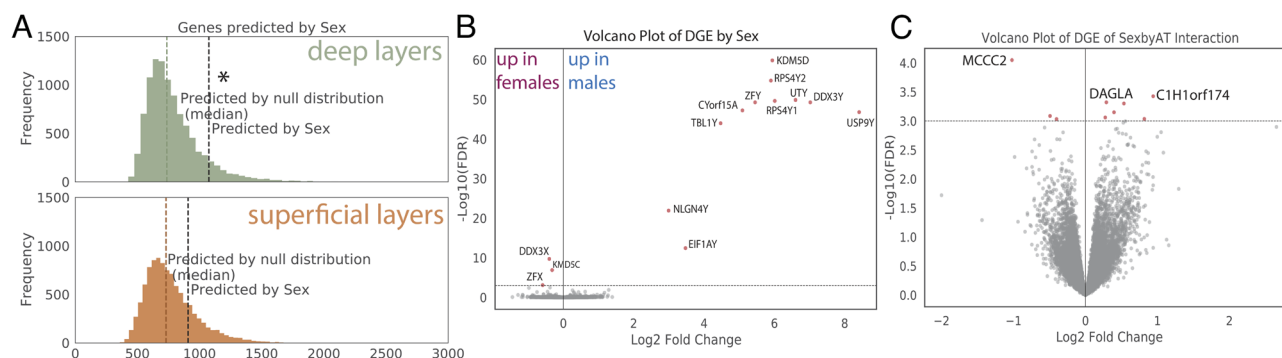

Fig. 4. Differential expression related to sex. Because the sample consisted of both males and females, sampled in the preadolescent age range, ordinary least squares linear regression was used to explore differential expression related to sex. (*A*) Permutation testing for sex as a predictor in the deep (green) and superficial (orange) datasets. The colored distribution reflects the shuffled null distribution, the colored dotted line represents the median of the distribution and the black line reflects the number of genes actually predicted by sex. * indicates an empirical P value < 0.05. (*B*) A volcano plot showing differential expression, with the log2 fold change score on the x axis and $-\log_{10}$(FDR-corrected P) on the y axis. The dotted line shows a cutoff of $-\log_{10}$(FDR-corrected P) < 0.001, with all genes passing that threshold shown in red dots. Genes in the upper left quadrant are up-regulated in females, while genes in the upper right quadrant are up-regulated in males. (*C*) A volcano plot showing the genes that are differentially expressed with respect to the interaction of AT and Sex in the deep layer dataset.

diacylglycerol lipase α (DAGLA), the main enzyme which produces the endocannabinoid 2-arachidonoyl glycerol (2-AG) (73), showed a sex by AT interaction (t = 3.68, uncorrected P = 0.0005), such that lower levels of this transcript were associated with AT in females but not males. Together, these results implicate novel molecules, including apoptotic factors in males and endocannabinoid signaling in females, in mediating AT-related sex differences in the frontal cortex.

Single Nuclear Sequencing. Our LCM findings implicate a variety of molecules, particularly those associated with GR signaling, in the deep layers of the pOFC in individual differences in AT. To better understand the cell type–specific composition of the pOFC as it relates to AT, we performed a systematic characterization of pOFC transcriptomic cell types. Subjects were selected from the high (n = 4, n = 2 male, n = 2 female) and low (n = 4, n = 2 male, n = 2 female) extremes of the n = 72 sample for single nuclear sequencing. Following quality control, which excluded nuclei with evidence of technical artifacts and background noise (74), greater than 5% of reads attributed to the mitochondrial genome, as well as nuclei identified as doublets using an automated identification algorithm (75), 57,290 nuclei remained for analysis, with an average of 58,269 ± 6,643.7 reads/nucleus and a median of 3,515 ± 831 genes/nucleus. Clustering revealed 23 transcriptomic

clusters, which were annotated based on previously established marker genes, shown in Fig. 5A. These clusters were consistent with prior single-cell transcriptomic studies in humans and rhesus monkeys (40), as well as studies characterizing the distribution of protein-based markers in interneuron populations (36). To determine whether there were any differences in composition between the high and low AT groups, we used scCODA (76) to analyze the cell type proportion across the groups. There were no significant differences in composition across all cell types, as can be seen in Fig. 5 B and E, demonstrating that differences in the AT phenotype do not likely arise because of an increased or decreased abundance of cells within pOFC circuits.

Further, we used the single nuclear data to characterize the localization of GR-associated transcripts, as well as other AT-associated transcripts that we highlighted above. Consistent with prior studies (77), the transcript for the GR was broadly expressed across transcriptomic clusters (Fig. 5B), while the transcript for CALD1 was primarily expressed in pyramidal neurons and some glial cells (Fig. 5C). *CALD1* and *NR3C1* were coexpressed in a subset of populations, particularly in clusters enriched for markers associated with pyramidal neurons in both the deep and superficial layers. Cell type–based localization of these and of other transcripts highlighted in the text is shown in Fig. 5C. Colocalization in deep layer cells was confirmed using
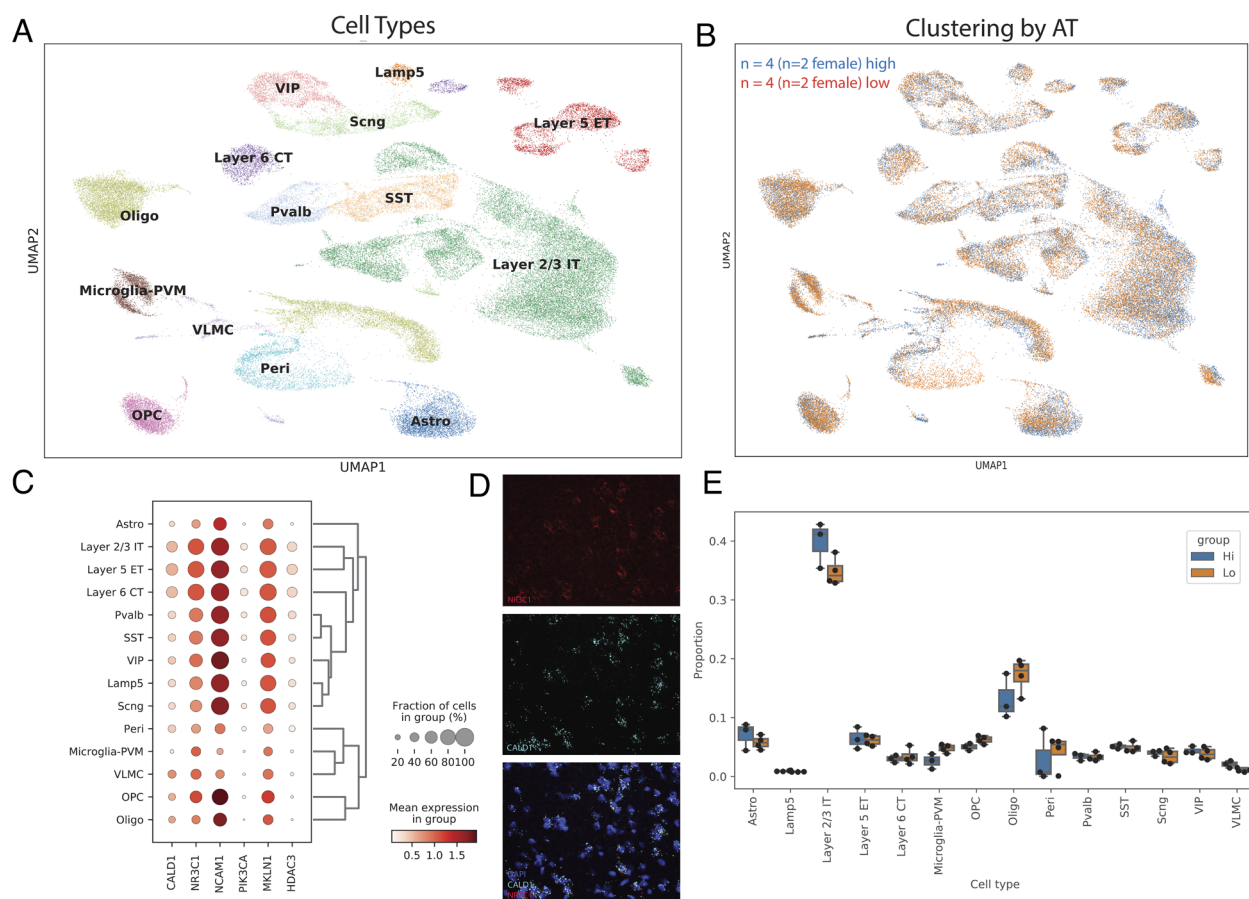

Fig. 5. Transcriptomic cell types and well as the distribution of GR-associated transcripts characterized by single-cell sequencing. (A) A plot showing the uniform manifold approximation embedding of cells characterized using single nuclear sequencing. Clusters were annotated based on the expression of known markers. (B) The same plot, showing whether the nuclei belonged to a subject in the high (blue) or low (orange) AT group. As can be seen in the figure, all clusters contain nuclei from subjects in both high and low groups. (C) A dot plot showing the expression of transcripts highlighted within the text. The dots on the dot plot represent the percentage of cells within the cluster that express the transcript in questions (0–100%), while the color intensity represents the average expression of the transcript in nuclei within the cluster. (D) RNAscope to characterize the distribution and overlap of *CALD1* and *NR3C1* in the deep layers of the pOFC in tissue collected from subjects that underwent single nuclear sequencing. As can be seen in the joined image, there is colocalization between expression of *NR3C1* and *CALD1*, confirming the single nuclear results. (E) A boxplot showing the relative proportion of cells in each annotated subtype with high in blue and low in orange, calculated using *scCODA* (76). No statistically significant differences in cell types were reported across high and low AT subjects.

RNAscope in tissue sections, as can be seen in the fluorescent images in Fig. 5*D*, with colabelling for *NR3C1*, *CALD1,* and DAPI. Across all cells expressing *NR3C1* or *CALD1*, the average puncta per cell was 8.01 (cv = 39.5%) and 3.23 (cv = 27%), respectively, reflecting the increased abundance of NR3C1 in the single nuclear data. While we were interested in using this RNAscope data to independently replicate the findings of associations between AT and these transcripts that we found in the larger LCM dataset, when we analyzed the LCM data from the 8 subjects in which single nuclear sequencing and RNAscope were performed, *NR3C1* (t= –0.13, FDR-corrected *P* = 0.995) and *CALD1* (t= –0.7, FDR-corrected *P* = 0.887) were not significantly differentially expressed with respect to AT. Thus, we would not expect to detect differential expression of these transcripts in this sample (n = 8) using either single nuclear sequencing or RNA scope. In addition, concerns based on the well-recognized issues with low coverage and a lack of distinction between biological and technical zeroes in single nuclear data precluded the use of this relatively small sample for differential expression analysis. Taken together, these issues highlight the importance of our large dataset, as well as the use of bulk methods which are less impacted by signal dropout for capturing dimensional variation related to AT.

Discussion

Early-life AT, when extreme and stable, is strongly associated with the emergence of anxiety and other stress-related disorders later in life. Our highly translational young rhesus monkey model for the early-life risk for stress-related psychopathology not only allows for understanding mechanisms related to vulnerability but also to developing strategies to enhance resilience. Using LCM methods paired with RNAseq in a large sample of preadolescent monkeys, we implicate several molecular systems in the pOFC in individual differences in AT. First, we show that neurons in deep versus superficial layers are substantially different in terms of their transcriptome. Permutation testing revealed that our predictors of interest had different relationships with gene expression across laminae, with a significant association between AT and transcriptome-wide expression in the deep, but not superficial layers. On the other hand, individual differences in threat-related cortisol in response to uncertain stress were associated with gene expression in both the deep and superficial layers.

Within our neural circuit model of AT, the pOFC has been considered a regulatory region for a variety of reasons. From an anatomical perspective, relative to other subregions of the frontal lobe, the pOFC is most densely connected with the amygdala and other limbic regions (21, 35, 36). In our large sample of n = 592 rhesus monkeys, threat-related metabolism in this region is associated with individual differences in AT. Perturbational studies suggest that the pOFC exerts a regulatory influence over other portions of the AT circuit, as lesions encompassing this region decrease AT and threat-related metabolism within components of the AT neural circuit (17).

Prior studies have linked acute and chronic stress via glucocorticoids to modulating neural plasticity processes in various brain regions, including the frontal cortex (78, 79). Such neuroplasticity processes in the pOFC could impact the regulation and expression of AT. For example, following exposure to chronic stress, rodents show decreased branching and dendritic complexity, particularly within the apical dendrites of layer II/III and V (56, 80, 81), which has been linked to signaling via the GR (82). Consistent with these findings, in the deep layers, AT is inversely associated with expression of *NR3C1,* the transcript encoding the

glucocorticoid receptor, and is positively associated with caldesmon an actin-binding protein (57) which is regulated by the GR. Caldesmon acts to stabilize the cytoskeleton and mediate the formation of dendritic spines (58–61). Because caldesmon is regulated by the GR and has a role in cytoskeleton stabilization, this raises the possibility that caldesmon might be a specific regulator of plasticity. Interestingly, caldesmon was only associated with AT in deep-layer neurons, which send projections to subcortical targets, suggesting that manipulations of this molecule could selectively modulate plasticity in these subcortically projecting neurons.

In addition to implicating the GR system, we also found evidence for a link between alterations in threat-related cortisol and BDNF signaling via enrichment analyses. This finding is consistent with our previous findings causally linking altered neurotrophin signaling in the dorsal amygdala to AT (69), as well as with investigations into the molecular basis for the effect of chronic stress on pyramidal neurons in the rodent frontal cortex (83, 84). Neurotrophins have a well-established link to synaptic plasticity (23), with links to the effects of stress on cortical circuit function and the actions of both slow and rapid-acting antidepressants (24, 68, 85, 86). This finding adds support to the developmental neuroplasticity hypothesis for AT and extends it to include the frontal cortex.

Much of the experimental evidence supporting a link between glucocorticoids, neurotrophic factors, and dendritic morphology comes from rodent paradigms involving either corticosterone administration (the rodent equivalent of cortisol) or chronic stress, which increases circulating corticosterone levels (24, 87, 88). Although these paradigms produce a phenotype that recapitulates certain elements of stress-related psychopathology (89, 90), they have not, until recently (see refs. 91 and 92), considered how preexisting temperamental dispositions predispose to vulnerability. In contrast to the stress induction required in rodent models, our NHP paradigm assesses preexisting individual differences in a stress-related temperament, AT, which is defined by variation in response to an uncertain stressor. These individual differences in the AT phenotype are associated with naturally occurring differences in neural circuit function, which are also stable across time (7). Both AT and its associated neural circuit function have been linked to genetic (7, 93, 94) and transcriptional (25, 69) variability. Thus, it is interesting that our work characterizing AT converges on findings from chronic stress models in rodents, extending the importance of glucocorticoids and neurotrophins to naturally occurring variability in a primate temperament associated with the risk of developing stress-related psychopathology.

Here, we provide a systematic characterization of the transcriptional profile of deep and superficial neurons in the pOFC, as well as the relationship between laminar transcription and AT. In addition to providing mechanistic insights into the molecular basis for the role of the pOFC in regulating AT, this work also identified potential molecular targets for the treatment and prevention of anxiety and depressive disorders. A leading candidate could be caldesmon, which could modulate GR-related plasticity within deep-layer neurons that project to subcortical structures involved in mediating AT. As in our previous work in the amygdala (69, 95), future work involving viral vector-mediated overexpression of this and other AT-related constructs in pOFC neurons will be important to better understand the causal relationship between neuroplasticity in the pOFC and AT. Such work in our highly translational rhesus monkey model for the early risk of developing stress-related psychopathology can guide the development of neurobiologically informed treatments for promoting resilience and

decreasing the substantial burden associated with stress-related psychopathology.

Author affiliations: [a]Neuroscience Training Program, University of Wisconsin, Madison, WI 53705; [b]Department of Psychiatry, University of Wisconsin, Madison, WI 53719; [c]Department of Cell Biology, State University of New York Downstate, New York, NY 11228; [d]Yale School of Medicine, Yale University, New Haven, CT 06510; [e]Department of Psychology and California National Primate Research Center, University of California, Davis, CA 95616; and [f]Wisconsin National Primate Research Center, University of Wisconsin, Madison, WI 53715

1. A. S. Fox *et al.*, Intergenerational neural mediators of early-life anxious temperament. *Proc. Natl. Acad. Sci. U.S.A.* **112**, 9118–9122 (2015).
2. R. Kotov *et al.*, The Hierarchical Taxonomy of Psychopathology (HiTOP): A dimensional alternative to traditional nosologies. *J. Abnorm. Psychol.* **126**, 454–477 (2017).
3. J. A. Clauss, J. U. Blackford, Behavioral inhibition and risk for developing social anxiety disorder: A meta-analytic study. *J. Am. Acad. Child Adolesc. Psychiatry* **51**, 1066–1075.e1 (2012).
4. M. J. Essex, M. H. Klein, M. J. Slattery, H. H. Goldsmith, N. H. Kalin, Early risk factors and developmental pathways to chronic high inhibition and social anxiety disorder in adolescence. *Am. J. Psychiatry* **167**, 40–46 (2010).
5. M. M. Kenwood, N. H. Kalin, Nonhuman primate models to explore mechanisms underlying early-life temperamental anxiety. *Biol. Psychiatry* **89**, 659–671 (2021).
6. N. H. Kalin, S. E. Shelton, Nonhuman primate models to study anxiety, emotion regulation, and psychopathology. *Ann. N. Y. Acad. Sci.* **1008**, 189–200 (2003).
7. A. S. Fox *et al.*, Intergenerational neural mediators of early-life anxious temperament. *Proc. Natl. Acad. Sci. U.S.A.* **112**, 9118–9122 (2015).
8. J. A. Oler *et al.*, Amygdalar and hippocampal substrates of anxious temperament differ in their heritability. *Nature* **466**, 864–868 (2010).
9. R. M. Birn *et al.*, Evolutionarily conserved prefrontal-amygdalar dysfunction in early-life anxiety. *Mol. Psychiatry* **19**, 915–922 (2014).
10. A. S. Fox, S. E. Shelton, T. R. Oakes, R. J. Davidson, N. H. Kalin, Trait-like brain activity during adolescence predicts anxious temperament in primates. *PLoS One* **3**, e2570 (2008).
11. N. H. Kalin, S. E. Shelton, A. S. Fox, T. R. Oakes, R. J. Davidson, Brain regions associated with the expression and contextual regulation of anxiety. *Biol. Psychiatry* **58**, 796–804 (2005).
12. A. V. Chavanne, O. J. Robinson, The overlapping neurobiology of induced and pathological anxiety: A meta-analysis of functional neural activation. *Am. J. Psychiatry* **178**, 156–164 (2021).
13. T. H. Ng, L. B. Alloy, D. V. Smith, Meta-analysis of reward processing in major depressive disorder reveals distinct abnormalities within the reward circuit. *Transl. Psychiatry* **9**, 1–10 (2019).
14. J. P. Gray, V. I. Müller, S. B. Eickhoff, P. T. Fox, Multimodal abnormalities of brain structure and function in major depressive disorder: A meta-analysis of neuroimaging studies. *Am. J. Psychiatry* **177**, 422–434 (2020).
15. M. M. Kenwood, N. H. Kalin, Nonhuman primate models to explore mechanisms underlying early-life temperamental anxiety. *Biol. Psychiatry* **89**, 659–671 (2021), 10.1016/j.biopsych.2020.08.028.
16. A. Etkin, A. Gyurak, R. O'Hara, A neurobiological approach to the cognitive deficits of psychiatric disorders. *Dialogues Clin. Neurosci.* **15**, 419–429 (2013).
17. M. M. Kenwood *et al.*, Prefrontal influences on the function of the neural circuitry underlying anxious temperament in primates. *Oxf. Open Neurosci.* **2**, kvac016 (2023).
18. A. S. Fox *et al.*, Orbitofrontal cortex lesions alter anxiety-related activity in the primate bed nucleus of stria terminalis. *J. Neurosci.* **30**, 7023–7027 (2010).
19. A. J. Shackman *et al.*, Neural mechanisms underlying heterogeneity in the presentation of anxious temperament. *Proc. Natl. Acad. Sci. U.S.A.* **110**, 6145–6150 (2013).
20. A. S. Fox, N. H. Kalin, A translational neuroscience approach to understanding the development of social anxiety disorder and its pathophysiology. *Am. J. Psychiatry* **171**, 1162–1173 (2014).
21. H. T. Ghashghaei, C. C. Hilgetag, H. Barbas, Sequence of information processing for emotions based on the anatomic dialogue between prefrontal cortex and amygdala. *NeuroImage* **34**, 905–923 (2007).
22. B. Zikopoulos, M. Höistad, Y. John, H. Barbas, Posterior orbitofrontal and anterior cingulate pathways to the amygdala target inhibitory and excitatory systems with opposite functions. *J. Neurosci.* **37**, 5051–5064 (2017).
23. H. Park, M. Poo, Neurotrophin regulation of neural circuit development and function. *Nat. Rev. Neurosci.* **14**, 7–23 (2013).
24. P. K. Parekh, S. B. Johnson, C. Liston, Synaptic mechanisms regulating mood state transitions in depression. *Annu. Rev. Neurosci.* **45**, 581–601 (2022).
25. R. Kovner *et al.*, Transcriptional profiling of primate central nucleus of the amygdala neurons to understand the molecular underpinnings of early life anxious temperament. *Biol. Psychiatry* **88**, 638–648 (2020).
26. M. E. Ritchie *et al.*, limma powers differential expression analyses for RNA-sequencing and microarray studies. *Nucleic Acids Res.* **43**, e47 (2015).
27. C. Nagy *et al.*, Single-nucleus RNA sequencing shows convergent evidence from different cell types for altered synaptic plasticity in major depressive disorder. bioRxiv [Preprint] (2018). https://doi.org/10.1101/384479.
28. H. R. Dueck *et al.*, Assessing characteristics of RNA amplification methods for single cell RNA sequencing. *BMC Genomics* **17**, 966 (2016).
29. S. L. Wolock, R. Lopez, A. M. Klein, Scrublet: Computational identification of cell doublets in single-cell transcriptomic data. *Cell Syst.* **8**, 281–291.e9 (2019).
30. B. Hie, B. Bryson, B. Berger, Efficient integration of heterogeneous single-cell transcriptomes using Scanorama. *Nat. Biotechnol.* **37**, 685–691 (2019).
31. F. A. Wolf, P. Angerer, F. J. Theis, SCANPY: Large-scale single-cell gene expression data analysis. *Genome Biol.* **19**, 15 (2018).
32. A. S. Fox, S. E. Shelton, T. R. Oakes, R. J. Davidson, N. H. Kalin, Trait-like brain activity during adolescence predicts anxious temperament in primates. *PLoS One* **3**, e2570 (2008).
33. A. S. Fox *et al.*, Central amygdala nucleus (Ce) gene expression linked to increased trait-like Ce metabolism and anxious temperament in young primates. *Proc. Natl. Acad. Sci. U.S.A.* **109**, 18108–18113 (2012).
34. M. Petrides, D. N. Pandya, Comparative cytoarchitectonic analysis of the human and the macaque ventrolateral prefrontal cortex and corticocortical connection patterns in the monkey. *Eur. J. Neurosci.* **16**, 291–310 (2002).
35. P. H. Rudebeck, E. A. Murray, Balkanizing the primate orbitofrontal cortex: Distinct subregions for comparing and contrasting values. *Ann. N. Y. Acad. Sci.* **1239**, 1–13 (2011).
36. H. Barbas, General cortical and special prefrontal connections: Principles from structure to function. *Annu. Rev. Neurosci.* **38**, 269–289 (2015).
37. M. Larkum, A cellular mechanism for cortical associations: An organizing principle for the cerebral cortex. *Trends Neurosci.* **36**, 141–151 (2013).
38. A. Bernard *et al.*, Transcriptional architecture of the primate neocortex. *Neuron* **73**, 1083–1099 (2012).
39. K. R. Maynard *et al.*, Transcriptome-scale spatial gene expression in the human dorsolateral prefrontal cortex. *Nat. Neurosci.* **24**, 425–436 (2021).
40. T. E. Bakken *et al.*, Comparative cellular analysis of motor cortex in human, marmoset and mouse. *Nature* **598**, 111–119 (2021).
41. A. Gidon *et al.*, Dendritic action potentials and computation in human layer 2/3 cortical neurons. *Science* **367**, 83–87 (2020).
42. M. E. Larkum, J. J. Zhu, B. Sakmann, Dendritic mechanisms underlying the coupling of the dendritic with the axonal action potential initiation zone of adult rat layer 5 pyramidal neurons. *J. Physiol.* **533**, 447–466 (2001).
43. M. E. Larkum, J. J. Zhu, B. Sakmann, A new cellular mechanism for coupling inputs arriving at different cortical layers. *Nature* **398**, 338–341 (1999).
44. K. Mozhui *et al.*, Strain differences in stress responsivity are associated with divergent amygdala gene expression and glutamate-mediated neuronal excitability. *J. Neurosci.* **30**, 5357–5367 (2010).
45. M. Muhia *et al.*, Muskelin regulates actin-dependent synaptic changes and intrinsic brain activity relevant to behavioral and cognitive processes. *Commun. Biol.* **5**, 589 (2022).
46. M. Nassan *et al.*, A genome wide association study suggests the association of muskelin with early onset bipolar disorder: Implications for a GABAergic epileptogenic neurogenesis model. *J. Affect. Disord.* **208**, 120–129 (2017).
47. B. W. Duncan, K. E. Murphy, P. F. Maness, Molecular mechanisms of L1 and NCAM adhesion molecules in synaptic pruning, plasticity, and stabilization. *Front. Cell Dev. Biol.* **9**, (2021).
48. M. E. Atz, B. Rollins, M. P. Vawter, NCAM1 association study of bipolar disorder and schizophrenia: Polymorphisms and alternatively spliced isoforms lead to similarities and differences. *Psychiatr. Genet.* **17**, 55–67 (2007).
49. L. H. Brennaman, P. F. Maness, "NCAM in neuropsychiatric and neurodegenerative disorders" in *Structure and Function of the Neural Cell Adhesion Molecule NCAM*, Advances in Experimental Medicine and Biology, V. Berezin, Ed. (Springer, 2010), pp. 299–317.
50. J. D. Gray, J. F. Kogan, J. Marrocco, B. S. McEwen, Genomic and epigenomic mechanisms of glucocorticoids in the brain. *Nat. Rev. Endocrinol.* **13**, 661–673 (2017).
51. P. Rhein *et al.*, Gene expression shift towards normal B cells, decreased proliferative capacity and distinct surface receptors characterize leukemic blasts persisting during induction therapy in childhood acute lymphoblastic leukemia. *Leukemia* **21**, 897–905 (2007).
52. K. V. Craenenbroeck, K. D. Bosscher, W. V. Berghe, P. Vanhoenacker, G. Haegeman, Role of glucocorticoids in dopamine-related neuropsychiatric disorders. *Mol. Cell. Endocrinol.* **245**, 10–22 (2005).
53. S. Cohen *et al.*, Chronic stress, glucocorticoid receptor resistance, inflammation, and disease risk. *Proc. Natl. Acad. Sci. U.S.A.* **109**, 5995–5999 (2012).
54. B. S. McEwen, J. H. Morrison, The brain on stress: Vulnerability and plasticity of the prefrontal cortex over the life course. *Neuron* **79**, 16–29 (2013).
55. C. L. Raison, A. H. Miller, When not enough is too much: The role of insufficient glucocorticoid signaling in the pathophysiology of stress-related disorders. *Am. J. Psychiatry* **160**, 1554–1565 (2003).
56. B. S. McEwen *et al.*, Mechanisms of stress in the brain. *Nat. Neurosci.* **18**, 1353–1363 (2015).
57. Y.-B. Yao, C.-F. Xiao, J.-G. Lu, C. Wang, Caldesmon: Biochemical and Clinical Implications in Cancer. *Front. Cell Dev. Biol.* **9**, (2021).
58. S. B. Kokate *et al.*, Caldesmon controls stress fiber force-balance through dynamic cross-linking of myosin II and actin-tropomyosin filaments. *Nat. Commun.* **13**, 6032 (2022).
59. T. Mayanagi, T. Morita, K. Hayashi, K. Fukumoto, K. Sobue, Glucocorticoid receptor-mediated expression of caldesmon regulates cell migration via the reorganization of the actin cytoskeleton. *J. Biol. Chem.* **283**, 31183–31196 (2008).
60. D. Tanokashira *et al.*, Glucocorticoid suppresses dendritic spine development mediated by down-regulation of caldesmon expression. *J. Neurosci.* **32**, 14583–14591 (2012).
61. F. Castellino, S. Ono, F. Matsumura, A. Luini, Essential role of caldesmon in the actin filament reorganization induced by glucocorticoids. *J. Cell Biol.* **131**, 1223–1230 (1995).
62. T. Mayanagi, K. Sobue, Diversification of caldesmon-linked actin cytoskeleton in cell motility. *Cell Adhes. Migr.* **5**, 150–159 (2011).
63. S. Arancibia *et al.*, Phosphatidylinositol 3-kinase interacts with the glucocorticoid receptor upon TLR2 activation. *J. Cell. Mol. Med.* **15**, 339–349 (2011).
64. M. W. Logue *et al.*, An analysis of gene expression in PTSD implicates genes involved in the glucocorticoid receptor pathway and neural responses to stress. *Psychoneuroendocrinology* **57**, 1–13 (2015).

65. V. Michopoulos, A. Powers, C. F. Gillespie, K. J. Ressler, T. Jovanovic, Inflammation in fear- and anxiety-based disorders: PTSD, GAD, and beyond. *Neuropsychopharmacology* **42**, 254–270 (2017).
66. M. Erta, A. Quintana, J. Hidalgo, Interleukin-6, a major cytokine in the central nervous system. *Int. J. Biol. Sci.* **8**, 1254–1266 (2012).
67. F. Caraci *et al.*, A key role for TGF-β1 in hippocampal synaptic plasticity and memory. *Sci. Rep.* **5**, 11252 (2015).
68. S. Deyama, R. S. Duman, Neurotrophic mechanisms underlying the rapid and sustained antidepressant actions of ketamine. *Pharmacol. Biochem. Behav.* **188**, 172837 (2020).
69. A. S. Fox *et al.*, Dorsal amygdala neurotrophin-3 decreases anxious temperament in primates. *Biol. Psychiatry* **86**, 881–889 (2019).
70. K. J. Zaccaria, D. C. Lagace, A. J. Eisch, J. S. McCasland, Resistance to change and vulnerability to stress: Autistic-like features of GAP43-deficient mice. *Genes Brain Behav.* **9**, 985–996 (2010).
71. M. M. McCarthy, A new view of sexual differentiation of mammalian brain. *J. Comp. Physiol. A Neuroethol. Sens. Neural. Behav. Physiol.* **206**, 369–378 (2020).
72. H. M. Belalcazar, E. L. Hendricks, S. Zamurrad, F. L. W. Liebl, J. Secombe, The histone demethylase KDM5 is required for synaptic structure and function at the Drosophila neuromuscular junction. *Cell Rep.* **34**, 108753 (2021).
73. B. C. Shonesy *et al.*, Genetic disruption of 2-arachidonoylglycerol synthesis reveals a key role for endocannabinoid signaling in anxiety modulation. *Cell Rep.* **9**, 1644–1653 (2014).
74. S. J. Fleming *et al.*, Unsupervised removal of systematic background noise from droplet-based single-cell experiments using Cell Bender. *Nat. Methods* **20**, 1323–1335 (2023).
75. C. S. McGinnis, L. M. Murrow, Z. J. Gartner, DoubletFinder: Doublet detection in single-cell RNA sequencing data using artificial nearest neighbors. *Cell Syst.* **8**, 329–337.e4 (2019).
76. M. Büttner, J. Ostner, C. L. Müller, F. J. Theis, B. Schubert, scCODA is a Bayesian model for compositional single-cell data analysis. *Nat. Commun.* **12**, 6876 (2021).
77. M. M. Sánchez, L. J. Young, P. M. Plotsky, T. R. Insel, Distribution of corticosteroid receptors in the rhesus brain: Relative absence of glucocorticoid receptors in the hippocampal formation. *J. Neurosci.* **20**, 4657–4668 (2000).
78. J. M. McKlveen *et al.*, Role of prefrontal cortex glucocorticoid receptors in stress and emotion. *Biol. Psychiatry* **74**, 672–679 (2013).
79. G. Turecki, M. J. Meaney, Effects of the social environment and stress on glucocorticoid receptor gene methylation: A systematic review. *Biol. Psychiatry* **79**, 87–96 (2016).
80. C. Liston *et al.*, Stress-induced alterations in prefrontal cortical dendritic morphology predict selective impairments in perceptual attentional set-shifting. *J. Neurosci.* **26**, 7870–7874 (2006).
81. J. J. Radley *et al.*, Repeated stress alters dendritic spine morphology in the rat medial prefrontal cortex. *J. Comp. Neurol.* **507**, 1141–1150 (2008).
82. B. Myers, J. M. McKlveen, J. P. Herman, Glucocorticoid actions on synapses, circuits, and behavior: Implications for the energetics of stress. *Front. Neuroendocrinol.* **35**, 180–196 (2014).
83. R. S. Duman, L. M. Monteggia, A neurotrophic model for stress-related mood disorders. *Biol. Psychiatry* **59**, 1116–1127 (2006).
84. S. Chiba *et al.*, Chronic restraint stress causes anxiety- and depression-like behaviors, downregulates glucocorticoid receptor expression, and attenuates glutamate release induced by brain-derived neurotrophic factor in the prefrontal cortex. *Prog. Neuropsychopharmacol. Biol. Psychiatry* **39**, 112–119 (2012).
85. P. C. Casarotto *et al.*, Antidepressant drugs act by directly binding to TRKB neurotrophin receptors. *Cell* **184**, 1299–1313.e19 (2021).
86. T. Yang *et al.*, The role of BDNF on neural plasticity in depression. *Front. Cell. Neurosci.* **14**, 82 (2020).
87. C. Liston, W.-B. Gan, Glucocorticoids are critical regulators of dendritic spine development and plasticity in vivo. *Proc. Natl. Acad. Sci. U.S.A.* **108**, 16074–16079 (2011).
88. R. M. Sapolsky, L. C. Krey, B. S. McEwen, Glucocorticoid-sensitive hippocampal neurons are involved in terminating the adrenocortical stress response. *Proc. Natl. Acad. Sci. U.S.A.* **81**, 6174–6177 (1984).
89. S. Antoniuk, M. Bijata, E. Ponimaskin, J. Wlodarczyk, Chronic unpredictable mild stress for modeling depression in rodents: Meta-analysis of model reliability. *Neurosci. Biobehav. Rev.* **99**, 101–116 (2019).
90. A. Gururajan, A. Reif, J. F. Cryan, D. A. Slattery, The future of rodent models in depression research. *Nat. Rev. Neurosci.* **20**, 686–701 (2019).
91. S. C. Tryon, I. M. Sakamoto, D. M. Kellis, K. F. Kaigler, M. A. Wilson, Individual differences in conditioned fear and extinction in female rats. *Front. Behav. Neurosci.* **15**, 740313 (2021).
92. T. M. Gruene, E. Roberts, V. Thomas, A. Ronzio, R. M. Shansky, Sex-specific neuroanatomical correlates of fear expression in prefrontal-amygdala circuits. *Biol. Psychiatry* **78**, 186–193 (2015).
93. J. Rogers, S. E. Shelton, W. Shelledy, R. Garcia, N. H. Kalin, Genetic influences on behavioral inhibition and anxiety in juvenile rhesus macaques. *Genes Brain Behav.* **7**, 463–469 (2008).
94. A. S. Fox *et al.*, Functional connectivity within the primate extended amygdala is heritable and associated with early-life anxious temperament. *J. Neurosci.* **38**, 7611–7621 (2018).
95. N. H. Kalin *et al.*, Overexpressing corticotropin-releasing factor in the primate amygdala increases anxious temperament and alters its neural circuit. *Biol. Psychiatry* **80**, 345–355 (2016).
96. M. Kenwood *et al.*, Laser capture microdissection and single nuclear sequencing from rhesus monkey posterior orbitofrontal cortex. BioProject. https://www.ncbi.nlm.nih.gov/bioproject/PRJNA1037749. Deposited 10 November 2023.

Supplemental Information

Methods
Laser Capture Microdissection
      Following euthanasia, fresh frozen tissue was collected, slabbed in accordance with the anatomical boundaries of regions of interest, and flash frozen in 2-methylbutane. Samples were stored at -80C until sectioning, which was performed in a cryostat at -10C. 14um sections were taken through the extent of the pOFC, encompassing primarily posterior area 13 and the orbital pro-isocortex (OPro) and were mounted on Leica PEN (Polyethylene napthalate) laser capture microdissection (LCM) slides (11532918; Leica, Wetzlar, Germany). To visualize the boundary between deep and superficial layers, adjacent section mounted on SuperFrost+ slides were stained using acetylcholinesterase. LCM slides were stained using a rapid stain for NeuN, which is selective for neuronal nuclei, described in more detail in (1).
      Dissection of deep (defined as layer V/VI) and superficial (defined as II/III) neurons were performed using a Leica LMD6500 laser capture microscope, with 1000 neurons dissected from each layer per animal from 5 to 6 individual slides. In order to confirm collection from the appropriate layer, images from the LCM slide were overlaid with the corresponding acetylcholinesterase slide in Adobe Illustrator CC 2014. Samples that fell outside of the region of interest were excluded. Cells from the deep and superficial layers were independently pooled within each animal. For the superficial layers, staining artifact around the edges of the tissue rendered it challenging to accurately collect neurons. Thus, neurons from superficial layers were only captured for 46 animals. RNA extractions were performed using the Qiagen RNeasy Plus Micro kit (74034; Qiagen, Hilden, Germany).

Statistical analysis: Model testing
      To avoid overfitting the statistical model, the variance in transcriptome-wide gene expression was tested against each nuisance variable of interest to determine statistical relevance. Correlations between nuisance variables of interest were also tested, to avoid multi-collinearity. Of the nuisance variables tested, RNA integrity number (RIN), Age at necropsy (Nx), Sex, and the number of cells collected described more variance in gene expression than a null distribution derived by permutation testing, and were thus included in the model. This model performed better (based on maximization of R^2 and minimization of the Bayesian information criterion) than models that did not include the relevant covariates in simulation testing. In all cases, the model was run in the superficial and deep layer data sets separately, with only the number of cells collected per layer differing between the two models.
      To test the effect of regional identity on gene and feature expression, the deep data set was subset to subject that also had cells collected from the superficial layers, yielding a total of 46 subjects. For gene level analyses, all counts summed across all features within a gene model. For feature level analyses, all counts considered separately for each feature. The final model is summarized below:

$$\hat{Y}_i = \hat{\beta}_0 + \hat{\beta}_1 Region_i + \hat{\beta}_2 Sex_i + \hat{\beta}_3 RIN_i + \hat{\beta}_4 AgeNx_i + \hat{\beta}_5 NumCellsCollected_i + \hat{\epsilon}_i$$

      The model was set up such that the main predictors of interest (AT, Cooing, Cortisol, Freezing) predicted either gene or features expression. Nuisance variables were included in the model based on the criteria discussed above. The final model is summarized below:

$$\hat{Y}_i = \hat{\beta}_0 + \hat{\beta}_1 MainPredictor_i + \hat{\beta}_2 Sex_i + \hat{\beta}_3 RIN_i + \hat{\beta}_4 AgeNx_i + \hat{\beta}_5 NumCellsCollected_i + \hat{\epsilon}_i$$

Where $\hat{Y}_i$ represented either the gene, isoform or count level data. P values were calculated for the beta weight for the main predictor using permutation testing, as in (1)

To test the main effect of sex, a model was used with sex as the main predictor, controlling for nuisance variance associated with RIN, age at necropsy and number of cells collected. Data from both the X and Y chromosome were included in the analyses. The final model is summarized below:

$$\hat{Y}_i = \hat{\beta}_0 + \hat{\beta}_1 Sex_i + \hat{\beta}_2 RIN_i + \hat{\beta}_3 AgeNx_i + \hat{\beta}_4 NumCellsCollected_i + \hat{\epsilon}_i$$

The output of each of these models can be explored in Supplemental Table 1. Additional models were run in limma, to test the interaction between AT and Sex, with the same covariates in the deep layer data set. The outputs of these models can also be found in Supplemental Table 1.

Single nuclear sequencing: Isolation and sequencing

The high and low group were also balanced for sex. As the slabs containing the pOFC were previously used for the OFC LCM study, we first verified the quality of the tissue and RNA for each subject. For each tissue slab, RNA quality was assessed, with a cutoff RIN of 6.0 for all slabs. A pilot snRNAseq run was performed with an adjacent section of cortical tissue for each subject and the yield and RNA quality were assessed for each subject. All subjects yielded sufficient nuclei for loading on a 10X chip, per manufacturer instructions, with quality RNA (RIN>5.0) for all samples.

First, all slabs containing the region of interest were sectioned and tissue sections were collected. The pOFC was dissected using a chilled scalpel at -20C. The dissected tissue was placed in a 1.5ml tube chilled on methanol and dry ice and then processed following protocols adapted from added to a glass dounce containing a solution of 1M Tris (pH 7.4), 1M NaCl, 1M MgCl$_2$, and nuclease free water. The tissue was dissociated with 10 strokes of a loose pestle and 15 strokes of a tight pestle, then transferred to a 15 mL Falcon tube. After 5 minutes of lysis with gentle agitation, a wash buffer containing 5% bovine serum albumin, glycerol, phosphate buffered saline (PBS) and RNAse inhibitor was added to the Falcon tube. The solution was then filtered using a 40-micron MACS filter, spun at 500g for 5 minutes at 4C, and resuspended in the wash buffer. After a second filtration with the 40-micron MACS filter, the solution was spun at 500g for 5 minutes at 4C and resuspended in 1mL of the wash buffer. A solution of iodixanol, nuclease free water, 2M KCl, 1M MgCl$_2$ and 1M Tricine K-OH, was added to the resuspended nuclei, for a final concentration of 25% iodixanol. This solution was added to a cushion of 30% iodixanol in nuclease free water, 2M KCl, 1M MgCl$_2$ and 1M Tricine K-OH, and then spun at 9,400g for 30 minutes at 4C. The resulting pellet was resuspended in PBS + 1% BSA and then isolated using a 10X 3' Single Cell v3.1 RNAseq kit.
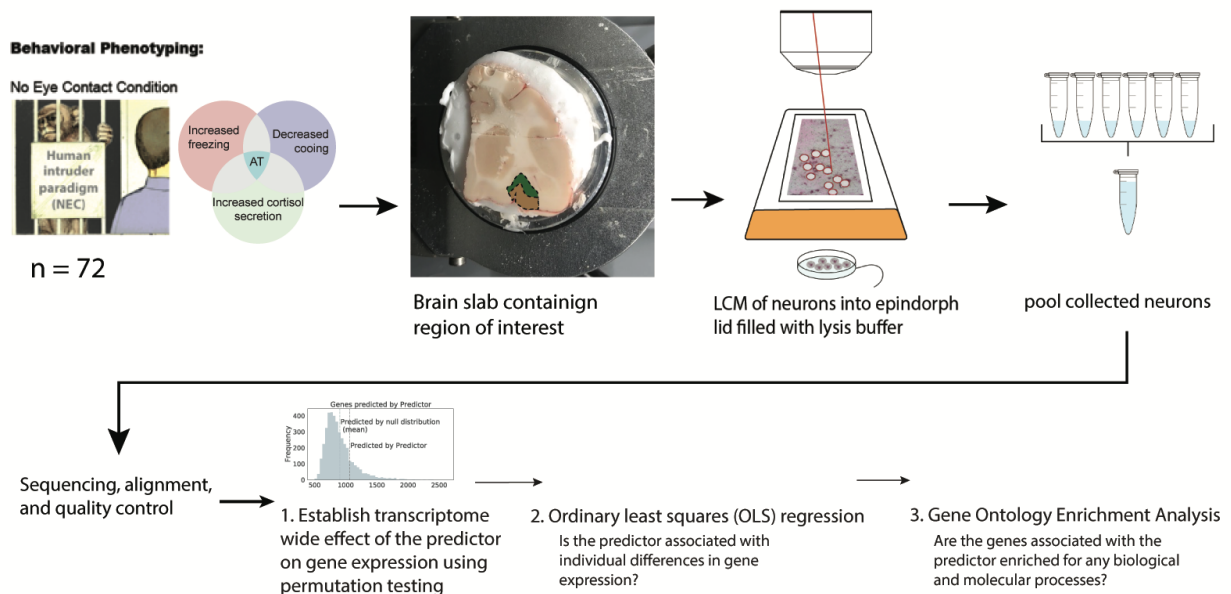
Single nuclear sequencing: Analysis

First, the general quality of the samples was compared. One sample had significantly fewer reads per nucleus (1,723 reads/nucleus, versus 3,546 reads/nucleus in the other data sets) and was therefore excluded from the analysis. Additional sequencing was performed for all samples in order to achieve sufficient read coverage on this outlying sample. However, after the additional sequencing, this sample still had significantly lower read coverage than the other samples (1,956 reads/nucleus, vs. 3,998 reads/nucleus in the other samples). The saturation was estimated to be similar across all samples, suggesting that there was lower diversity within sample 49. Thus, it is likely that there is some technical factor that is responsible for the discrepancy in read totals and thus this sample was excluded from analyses. Reads for all other samples reflect the combined data from both sequencing runs. Raw reads were filtered using CellBender (2), to remove contamination associated with background RNA. The remaining

samples were filtered to remove any nuclei whose count number fell within the bottom 5% of the counts distribution, as these low count barcodes are likely to reflect technical noise resulting from ambient RNA. The percentage of counts that could be attributed to the mitochondrial genome was calculated for each nucleus and nuclei with over 5% of counts attributed to the mitochondrial genome were excluded. Scrublet (3) was used to exclude barcodes that likely reflected the transcriptional profile of doublets, based on simulated data. Following quality control, 57,290 nuclei remained for analysis, with an average of 58,269 +/- 6,643.7 reads/nucleus and a median of 3,515 +/- 831 genes/nucleus.

The data were then normalized using the *scanpy* package (4) and genes that displayed high variability across the nuclei were selected. Data were then scaled, such that the mean expression and variance of each gene were 0 and 1, respectively, to ensure all genes are equally weighted for dimensionality reduction. First, linear dimensionality reduction was performed using principal components analysis (PCA) to reveal global sources of variance with the dataset and to initialize other clustering algorithms, which can be substantially more computationally intensive. The number of highly informative PCs was determined using the Jackstraw Method. Based on this cutoff, the first 50 PCs were selected for clustering. Clustering was then performed on the full data set in Seurat and clusters were divided using the Leiden method. This approach yielded 23 clusters across the full data set.
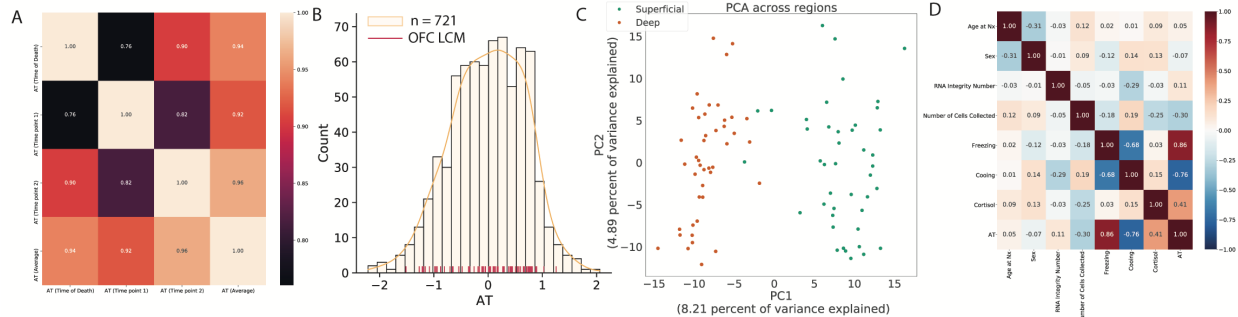
Non-linear dimensionality reduction was then performed using uniform manifold approximation (UMAP), which embeds the nuclei on a manifold, attempting to maximize the proximity of individual nuclei in lower dimensional space. To determine marker genes for each cluster detected using the Leiden method, differential expression (DE) was performed between clusters, based on the log2 fold change in gene expression between clusters. Clusters were annotated using Azimuth (https://satijalab.github.io/azimuth/index.html), using the human motor cortex as a reference.
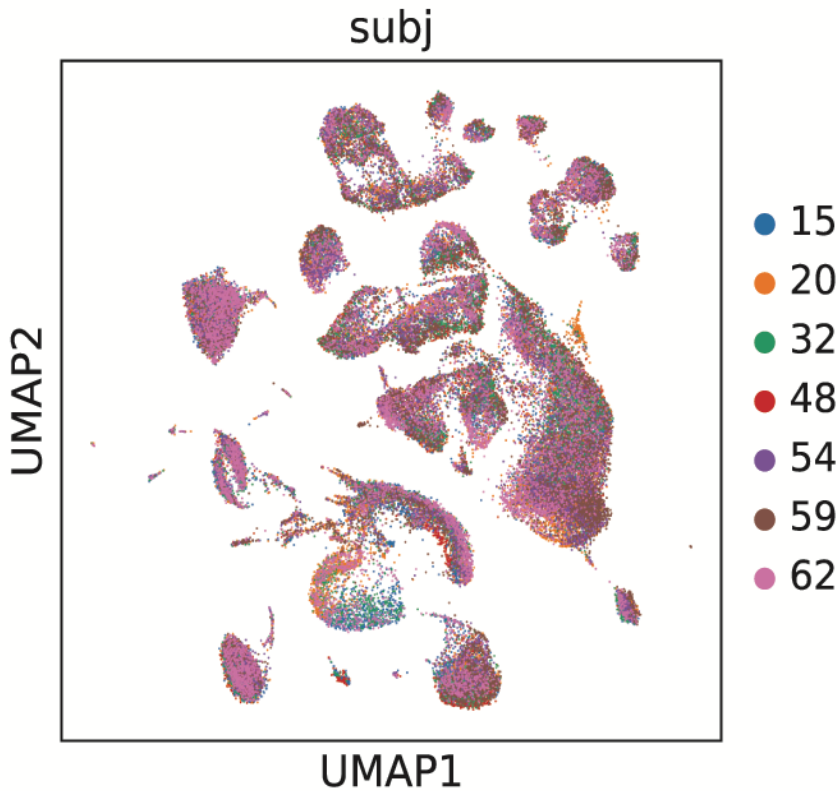
Supplemental Figure Captions

Supplemental Figure 1: A schematic showing the experimental pipeline. Subjects were screened using a 30-minute exposure to the No Eye Contact (NEC) condition of the Human Intruder Paradigm (HIP), during which AT is assessed by creating a combined score of freezing, the inverse of cooing during the exposure and cortisol levels in blood taken after the exposure. Brains were collected, flash frozen and section on a microtome. A rapid stain for NeuN was

used to visualize neuronal nuclei, which were subsequently microdissected using laser capture microdissection methods. Neurons were pooled across several sections and sequenced. Following alignment, samples were tested on a variety of quality control metrics. Permutation analyses were performed by shuffling the predictor of interest 10,000 times to generate a null distribution. Predictors were considered to have evidence of an omnibus effect if the actual number of genes associated with the predictor was more extreme than 5% of the simulations, reflecting an empirical $p < 0.05$. For predictors that passed this threshold, ordinary least squares regression was used to generate a list of genes that showed a linear relationship with the predictor of interest. Individual genes were interpreted, as well as ontology testing on genes surviving correction at $p < 0.05$ uncorrected.

Supplemental Figure 2: Sample and model characterization. A) AT scores are stable across time, with correlation coefficients between 0.76 and 0.96. The heatmap shows the correlations between AT at the time of necropsy, used as the main predictor of interest in the statistical models and AT scores taken at two other time point for a subset of the n=72 animals, as well as the average across all AT scores. B) A rugplot showing the distribution of the AT scores calculated within the n=71 animals that formed part of the LCM study (burgundy) relative to a large sample of n=721 animals (yellow) that have been characterized for AT. As can be seen in the figure, the n=71 are evenly distributed across the wider sample range, supporting that this is representative sample. D) A principal components analysis showing the main source of variance within the overlap data set, where the n=43 subjects with data collected from both deep and superficial layers are included. Points are colored by laminar origin, showing that neurons collected from the deep and superficial layers cluster separately. C) Correlation between AT, its components and the variables included in the statistical model. As can be seen in the heatmap, the nuisance variables are not strongly correlated with any predictor of interest. As is expected based on previous work (5, 6), freezing and cooing are inversely correlated, while cortisol is not correlated with freezing or cooing.

Supplemental Figure 3: UMAP clustering colored based on subject. This clustering demonstrates that all subjects contribute to all clusters and are evenly intermixed.

Supplemental References

1. R. Kovner, *et al.*, Transcriptional Profiling of Primate Central Nucleus of the Amygdala Neurons to Understand the Molecular Underpinnings of Early Life Anxious Temperament. *Biol. Psychiatry* **0** (2020).

2. S. J. Fleming, *et al.*, Unsupervised removal of systematic background noise from droplet-based single-cell experiments using CellBender. *Nat. Methods*, 1–13 (2023).

3. S. L. Wolock, R. Lopez, A. M. Klein, Scrublet: Computational Identification of Cell Doublets in Single-Cell Transcriptomic Data. *Cell Syst.* **8**, 281-291.e9 (2019).

4. F. A. Wolf, P. Angerer, F. J. Theis, SCANPY: large-scale single-cell gene expression data analysis. *Genome Biol.* **19**, 15 (2018).

5. A. J. Shackman, *et al.*, Neural mechanisms underlying heterogeneity in the presentation of anxious temperament. *Proc. Natl. Acad. Sci. U. S. A.* **110**, 6145–6150 (2013).

6. A. S. Fox, *et al.*, Intergenerational neural mediators of early-life anxious temperament. *Proc. Natl. Acad. Sci.* **112**, 9118–9122 (2015).